Journal of the American Chemical Society 139.29 (2017): 10079-10086

DOI: https://doi.org/10.1021/jacs.7b05182

Ionic Conductivity and Potential Application for Fuel Cell of a Modified Imine-based Covalent Organic Framework

Carmen Montoro,[†] David Rodríguez-San-Miguel,[†] Eduardo Polo,[†] Ricardo Escudero-Cid,[‡] Maria Luisa Ruiz-González,[£] Jorge A. R. Navarro,[§] Pilar Ocón[*‡] and Félix Zamora[*†,∥]

[†] Departamento de Química Inorgánica, Institute for Advanced Research in Chemical Sciences (IAdChem) and Condensed Matter Physics Center (IFIMAC). Universidad Autónoma de Madrid. 28049 Madrid, Spain.

[‡] Departamento de Química Física Aplicada. Universidad Autónoma de Madrid. 28049 Madrid, Spain.

[£] Departamento de Química Inorgánica, Universidad Complutense de Madrid, 28040 Madrid, Spain.

[§] Departamento de Química Inorgánica. Universidad de Granada. 18071 Granada, Spain.

[∥] Instituto Madrileño de Estudios Avanzados en Nanociencia (IMDEA-Nanociencia), Cantoblanco, Madrid E-28049, Spain.

Keywords: Covalent Organic Framework, ionic conductivity, porous crystalline materials, proton exchange membranes, thin films.

ABSTRACT: We present the novel potential application of imine-based Covalent Organic Frameworks (COFs), formed by the direct Schiff reaction between 1,3,5-tris(4-aminophenyl)benzene and 1,3,5-benzenetricarbaldehyde building blocks in *m*-cresol or acetic acid, named as **RT-COF-1** or **RT-COF-1Ac**/**RT-COF-1AcB**. The post-synthetic treatment of **RT-COF-1** with LiCl leads to the formation of **LiCl@RT-COF-1**. The ionic conductivity of this series of polyimine COFs has been characterized at variable temperature and humidity, using electrochemical impedance spectroscopy. **LiCl@RT-COF-1** exhibits a conductivity value of 6.45×10^{-3} S cm^{-1} (at 313 K and 100 % relative humidity) which is among the highest values so far reported in proton conduction for COFs. The mechanism of conduction has been determined using ^{1}H and ^{7}Li Solid-State Nuclear Magnetic Resonance Spectroscopy. Interestingly, these materials, in the presence of controlled amounts of acetic acid and under pressure, show a remarkable processability that give rise to quasi-transparent and flexible films showing in-plane structural order as confirmed by X-ray crystallography. Finally, we prove that these films are useful for the construction of proton exchange membrane fuel cells (PEMFC) reaching values up to 12.95 mW cm^{-2} and 53.1 mA cm^{-2} for maximum power and current density at 323 K, respectively.

INTRODUCTION

The world's total increase in energy consumption linked to the decrease of natural resources prompt the search of new forms of energy capable of satisfying these needs. Fuel cell technology offers many advantages compared to conventional power sources, such as high conversion efficiency, environmentally friendly working and low maintenance and portability.[1,2] Indeed, proton exchange membrane fuel cells (PEMFC) are one of the best options that can be found in this field. An ideal ion exchange membrane should have, among other features, high ionic conductivity, zero electronic conductivity, low gas permeability, good chemical and thermal stability under fuel cell operating conditions as well as a good thin-film processability. Taking into account all these requirements, one of the most popular materials used as an electrolyte membrane is Nafion®, which achieves a proton conductivity of 10^{-1} S cm^{-1} after humidification.[3] However, Nafion® presents some limitations related to production cost, safety and environmental concerns that have to be solved with alternative membranes.[4,5] In this regard, crystalline porous materials have attracted great interest as proton-conducting materials.[6] Among them, Covalent Organic Frameworks (COFs) based on Schiff condensation reactions[7] are potential candidates that could fulfill these requirements.[6,8-11] Indeed, crystalline laminar COFs can be considered promising platforms for the formation of ion conductive membrane materials as a result of the rational design of their structures, their easy functionalization and their inherent properties like low mass density, high thermal and chemical stability and permanent porosity.[4,11-16] Furthermore, despite a few COFs showing ionic conductivities as high as 3.96×10^{-2} S cm^{-1}, at room temperature,[17-19] convenient methodologies of synthesis, processing and integration of these materials on supports are on their infancy.[5,20-22] In this sense, we have recently published the room temperature one-pot condensation reaction of 1,3,5-tris(4-aminophenyl)benzene with 1,3,5-benzenetricarbaldehyde to yield **RT-COF-1** and **RT-COF-1Ac**.[20,23] In view of the easy formation and good chemical and thermal stability of the above materials, we have now prepared two novel variants, namely **RT-COF-1AcB** and **LiCl@RT-COF-1** (Figure 1). Moreover, we have studied the impact of synthetic conditions and hosted guest molecules on the ionic conductivity and processability as fuel cell polymer electrolyte membranes for the whole COF material series.

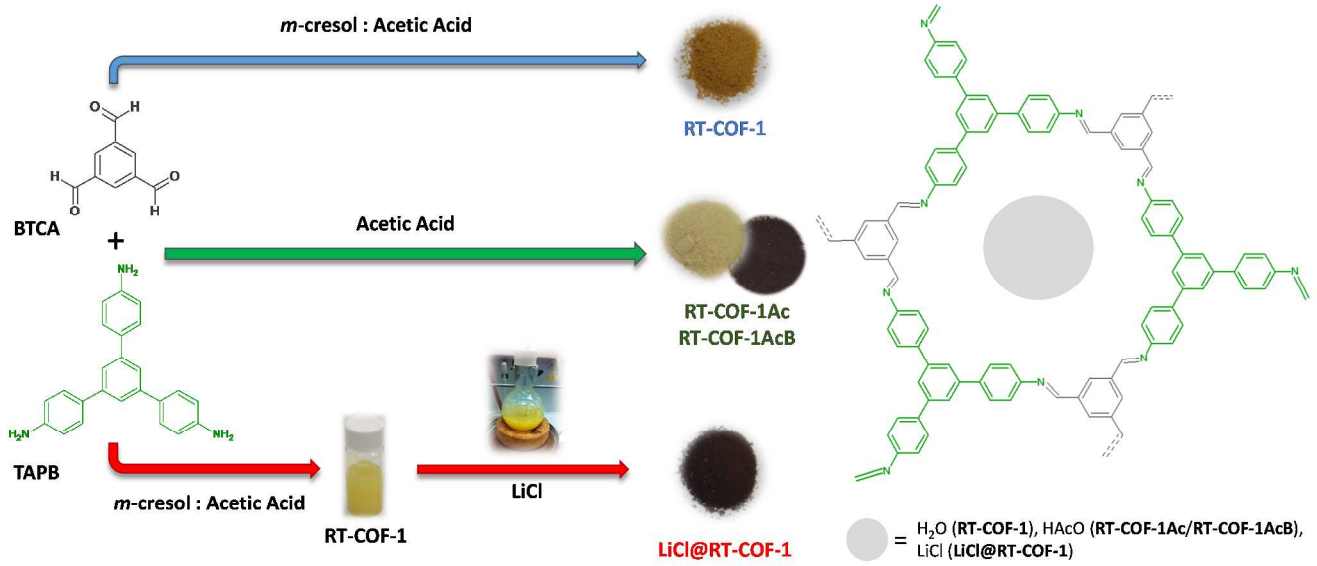

Figure 1. Schematic representation of the synthesis and structure of **RT-COF-1**, **RT-COF-1Ac, RT-COF-1AcB** and **LiCl@RT-COF-1** materials. The gray circle represents the different guest molecules trapped in the pore windows of **RT-COF** materials.

RESULTS AND DISCUSSION

Synthesis and Characterization. RT-COF-1 and **RT-COF-1Ac** were prepared according to published procedures reported previously by us.[19,22] **RT-COF-1AcB** is obtained by the direct reaction, at room temperature, between 1,3,5-tris(4-aminophenyl)benzene (TAPB) and 1,3,5-benzenetricarbaldehyde (BTCA) using acetic acid as solvent and catalyst (Figure 1). The viscous gel so-obtained was washed with tetrahydrofuran and isolated by filtration. The resulting solid was dried under open atmosphere over 2 days. The comparison between the spectroscopic features of **RT-COF-1**, **RT-COF-1Ac** and **RT-COF-1AcB** shows that all of them are very similar with the only difference of the guest molecules trapped in the porous structure, water for **RT-COF-1** as well as acetic acid for **RT-COF-1Ac** and **RT-COF-1AcB**. The gentle drying applied to the **RT-COF-1AcB** material facilitates the permanence of a greater number of acetic acid guest molecules, namely 3.5 molecules per formula unit, as derived from elemental analysis, IR spectra (Figure S1), Solid State ^{13}C CP-MAS NMR Spectra (Figure S7) and thermogravimetric analysis (Figure S11). Moreover, the presence of a higher amount of acetic acid is also manifested by an appreciable color change from yellow to dark red.

Nitrogen adsorption data and pore size distribution are gathered in Figure S13. The results are in agreement with the structural model of **RT-COF-1** already reported by us (pore windows of 1.2 nm).[20] Indeed, DFT calculations of pore size distribution are indicative of pore size maximum of 1.2 nm for **RT-COF-1Ac** and ~1.1 nm for **RT-COF-1AcB** (Figure S13b and c). It is also interesting to highlight the increase in BET surface and pore volume on passing from **RT-COF-1** (330 m^2 g^{-1}, 0.1 cm^3 g^{-1}) to **RT-COF-1Ac** (750 m^2 g^{-1}, 0.2 cm^3 g^{-1}) which should be related to the benefit of the acetic acid catalyst on the imine bond formation reversibility. It should be noted, however, that a further increase in acetic acid concentration on **RT-COF-1AcB** material synthesis (glacial acetic acid) gives rise to a decrease in specific surface area adsorption capacity (550 m^2 g^{-1}, 0.19 cm^3 g^{-1}) and pore size (~1.1 nm). It could be related to an increased material ordering related to the enhanced bond formation reversibility leading to a highly crystalline material (Figure S15) exhibiting a type I adsorption isotherm with a sharp knee at $P/P^0 < 0.1$ characteristic of a microcrystalline microporous material. On the other hand, the incorporation of LiCl ion pairs in the structure of **LiCl@RT-COF-1** leads to a complete loss of N_2 adsorption capacity that is indicative of accommodation of these guest molecules in the pore windows of this material.

The study of the chemical stability of **RT-COF-1Ac**, which exhibits the basic structural features of the whole material series, was essayed by exposing it to acidic (HCl, 12 M) and basic (NaOH, 14 M) concentrated aqueous solutions at room temperature. X-ray powder diffraction (Figure S4) and thermogravimetric analyses confirmed that the framework integrity remains unchanged after these treatments. Therefore, it can be stablished that all materials are chemically stable under highly demanding chemical conditions.

Interestingly, the gel nature of **RT-COF-1** facilitated its post-synthetic modification by treatment with an aqueous solution of LiCl at room temperature for 24 h (Figure 1). The study of the isolated **LiCl@RT-COF-1** (Figure S16) shows that the incorporation of Li^+, Cl^- ion pairs does not affect the original structure as evidenced by the retention of the characteristic **RT-COF-1** PXRD pattern (Figure S2) and similar spectroscopic features and thermal stability (Figure S1 and S12).[8] ICP-MS analysis shows a Li:Cl:N 1:2.5:10 ratio confirming the actual incorporation of LiCl into the material. Moreover, the loss of pore accessibility, as concluded from N_2 adsorption isotherms, after LiCl infiltration is indicative of the inclusion into the COF pore windows (Figure S13). The observed deficiency of Li^+ ions may arise from a probable partial protonation of imine groups.

Importantly, the analysis of the N 1s spectrum obtained by XPS shows two components at 397.00 and 398.23 eV which are assigned, respectively, to free imine nitrogen atoms of the **RT-COF-1** framework and the imine nitrogen atoms interacting with $[Li(OH_2)_4]^+$ ions and/or protons. The observed ratio 4:1 between the two N peaks indicates that most of the N atoms are not involved in H-bonding interactions. In order to confirm this hypothesis, we have also carried out solid state ^{7}Li MAS NMR studies with **LiCl@RT-COF-1** at 22 % and 100 % RH (Figure S10). Thus, the spectrum recorded at 22 % relative humidity (RH) shows a broad peak that can be deconvoluted in two components, 0.00 and 0.23 ppm. The one at 0.00 ppm, which is less intense, is assigned to free $[Li(OH_2)_4]^+$, while the more prominent one at 0.23 ppm could be due to $[Li(OH_2)_4]^+$ interacting with the imino atoms of the **RT-COF-1** framework. The ^{7}Li MAS NMR spectrum of **LiCl@RT-COF-1** at 100 % RH shows just a sharp signal at 0.00 ppm which can be assigned to free $[Li(OH_2)_4]^+$ ions. These results agree with those found in the N 1s XPS spectrum and allow us to conclude that $[Li(OH_2)_4]^+$ is located into the **RT-COF-1** cavities with the $[Li\text{-}O\text{-}H\cdots N_{imino}]$ H-bonding interactions with the imino nitrogens being highly dependent on the environmental moisture values.

RT-COF-1Ac was studied by TEM in an aberration corrected microscope at 60 kV in order to avoid sample degradation under the electron beam (SI). A typical low magnification image is shown in Figure 2a. It evidences the presence of COF multilayers giving rise to two kinds of stacking (marked in Figure 2a): *i*) a random one, similar to those described in turbostratic carbon, leading to an amorphous appearance (see the lower part of figure 2a) and *ii*) a distorted one but with a certain degree of coherence leading to crystalline domains exhibiting an hexagonal ordering. These features can be better observed in the high resolution image shown in Figure 2b. Indeed, two microstructural features, A and B, are observed. On one side, the already mentioned hexagonal lattice (see area A), with apparent periodicities of 0.25 × 0.25 nm. This periodical distance is related to the average C-C distance in the **RT-COF-1** lattice.[19] Nevertheless, a more careful inspection allows visualizing a diffuse framework (better observed in the enhanced detail in Figure 2c) of 1.2 × 1.2 nm dimensions, which fit well with the pore size of **RT-COF-1**.[19] The FTT in this area is in agreement to this description suggesting that, even when the stacking ordering is not complete, every single layer must be closely orientated along the [001] zone axis (pore direction).

On the other side, distances of 0.35 nm in one direction have been measured in areas similar to B, as can be better observed in the enhanced detail depicted in Figure 2d. This periodicity is in agreement to the interlayer separation in **RT-COF-1**, *i.e.*, along the [001] direction. These features are representative of the COF material, as can be observed in other similar images supplied in Figure S15, supporting the average structure deduced by powder X-ray diffraction[19] but showing the presence of different stacking ordering arrangements in agreement to related materials.[24,25]

On the other hand, water adsorption isotherms are indicative of increasing hydrophilicity along the **RT-COF-1**, **RT-COF-1Ac**, **LiCl@RT-COF-1** series (Figure 3). This result agrees with the highly hydrophilic nature of Li^+ cations.[26] The high water vapor uptake capacity of **LiCl@RT-COF-1** at elevated relative pressures, namely, 635 $cm^3\ g^{-1}$ at P/P^0 = 0.9 (90 % RH) and the presence of Li^+ cations within the pores make this material an excellent ion conductor candidate.

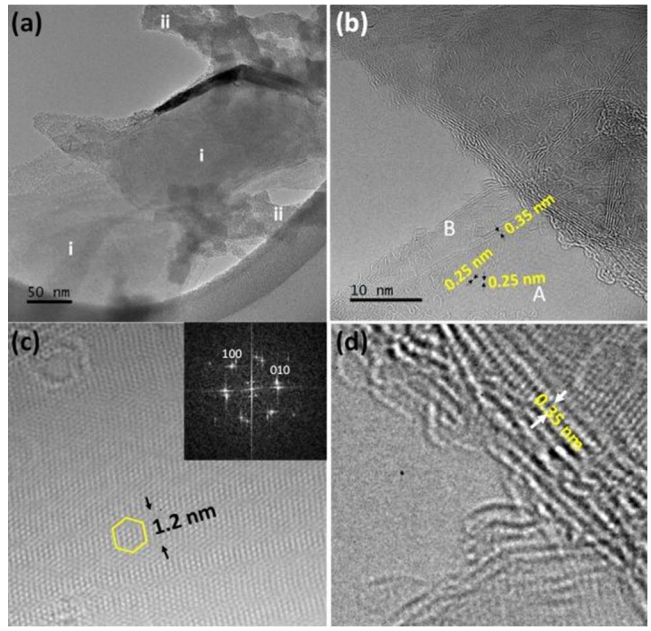

Figure 2. (a) Characteristic low magnification TEM image of **RT-COF-1Ac** showing areas of different type of layer stacking, (i) and (ii), described in the main text; (b) HRTEM image typical of the type (ii) stacking. Two different areas (A and B) are evident; (c) Enhanced detail of zone A and its corresponding FFT; (d) Enhanced detail of zone B.

Ionic Conductivity. The **RT-COF-1Ac**, **RT-COF-1AcB** and **LiCl@RT-COF-1** materials were processed in the form of films of 0.01-0.03 cm thickness and 13 mm of diameter (SI section II) in order to evaluate their ionic conductivity. In the case of **RT-COF-1** only pressed pellets could be obtained. The morphology and roughness of the obtained films were examined by field emission scanning electron microscopy (FESEM) and atomic force microscopy (AFM) (Figures S19-S21). **RT-COF-1Ac** and **RT-COF-1AcB** films micrographs showed that they have similar aspect but larger holes are present in the latter material. Noteworthy, **LiCl@RT-COF-1** film seems to be more uniformly compacted than the others, although the grain boundaries are larger and form long and deep cracks. An outstanding feature observed in the processed **RT-COF-1Ac** material is its ability to form quasi-transparent and flexible-thin films (Figure S3) while these features are not observed in the other two films. In this sense, it is worth highlighting the importance of the limited number of acetic acid molecules during material processing, which leads to a quasi-transparent and flexible thin film under pressure. This result might be related to the possible role of acetic acid as a catalyst under the high pressure conditions facilitating the polyimine condensation reaction at the grain boundaries (random quantities of amine and aldehyde groups are present at the defective edges) of the COF-polyimine layers giving rise to the formation of larger aggregates. Alternatively, acetic acid molecules may play an important role connecting the edges of the

COF-polyimine layers by H-bonding formation between the amine and aldehyde groups present at the defective COF-polyimine edges. Thus, pressuring microcrystalline powders of **RT-COF-1Ac** up to *ca*. 300 MPa leads to the formation of thin, flexible and transparent films. By contrast, lower pressures, namely, 15-200 MPa, give rise to conventional thicker films. To gain further knowledge on whether there is any structural change upon pressurization, we have acquired the X-ray diffraction patterns of the pellet and film of **RT-COF-1Ac**, using CuK_{α} radiation under transmission and reflection modes, employing a single crystal Bruker D8 Venture instrument (Figure S3). The results show that the PXRD pattern coincides with those derived from the **RT-COF-1** structure prior to being pressed.[8] However, the results indicate that while the application of 15 MPa does not lead to any preferential orientation, the formation of the **RT-COF-1Ac** film seems to give rise to a certain degree of preferential orientation, as manifested by higher intensity of the [100] reflection in the transmission mode. Nevertheless, the preferential orientation is significantly lower than those found by Uribe *et al.*[17] in related imine COFs.

The ionic conductivity of the as-thin film processed materials has been evaluated using electrochemical impedance spectroscopy (EIS) from 298 to 313 K and at two different relative humidities (RH), 22 and 100 %. The conductivity values have been calculated using the expression $\sigma = L/(R \times A)$, where σ is the conductivity value (S cm^{-1}), L the thickness of the sample (cm), A is the electrode area (cm^2) and R (Ω) is the electrolyte resistance corresponding to the real Z´ Nyquist plot.

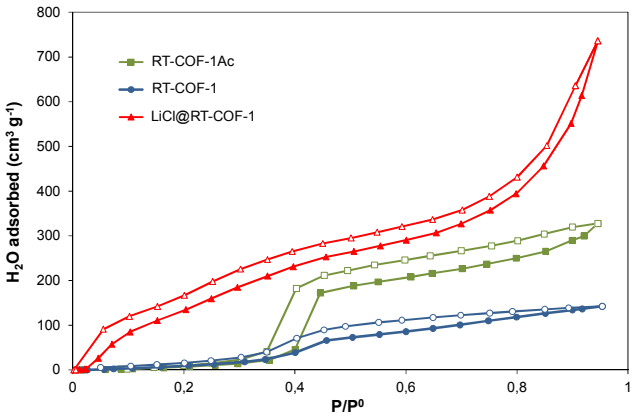

Figure 3. Water vapor adsorption isotherms (298 K) of **RT-COF-1**, **RT-COF-1Ac** and **LiCl@RT-COF-1** materials. Filled and open symbols correspond to adsorption and desorption processes, respectively.

The four materials showed negligible conductivity values of *ca*. 10^{-9} - 10^{-10} S cm^{-1} at 22 % RH in the temperature range studied, suggesting that there is no significant ionic transport. Moreover, this result might also indicate that the water molecules present in the structure are trapped in the pores, being unable to provide a continuous proton hopping pathway. However, as far as the humidity increases up to a maximum value of 100 % RH, the conductivity values of the four materials increase notoriously. This is clearly shown in Figures 4 and S22 in which the arc extrapolation to the axis Z' decreases upon increasing the wetting time in all cases. **LiCl@RT-COF-1** film exhibits the highest conductivity value of 6.45×10^{-3} S cm^{-1} that is followed by **RT-COF-1AcB** and **RT-COF-1Ac** films with values of 5.25×10^{-4} S cm^{-1} and 1.07×10^{-4} S cm^{-1}, respectively. The **RT-COF-1** pellet exhibits the lowest value of 1.83×10^{-5} S cm^{-1} (Table 1). These results are in good agreement with the materials hydrophilicity as concluded from water adsorption isotherms (see above). Additionally, the Nyquist plots of the **RT-COF-1** pellet and **RT-COF-1Ac**, **RT-COF-1AcB** and **LiCl@RT-COF-1** films confirm that the proton conductivity values are strongly dependent on materials hydration, with a significant enhancement of the conductivity values with increasing wetting time (Figure 4). These results clearly indicate that the combination of water and guest ion pairs (LiCl, HAcO) play a significant role in the proton conduction pathways of these porous materials. Consequently, the higher the hydrophilicity of the COF porous channels the more efficient the proton and Li^+ transport.

Remarkably, the conductivity value obtained for the **LiCl@RT-COF-1** film at 313 K and 100 % RH is among the highest reported so far for both COFs and MOFs under similar operative conditions.[4,18,27-33] In this sense, despite it being still very far from outperforming the ionic conductivity properties of Nafion®, the use of imine-based COFs would overcome some limitations of this material in relation to its high manufacturing cost, difficult synthesis strategy and deactivation above 353 K. Moreover, it is well-known that COFs can be synthesized by different simple procedures and in general show extremely robust chemical and thermal stability thanks to the covalent bond formation. On the other hand, it should also be noted that the best conductivity values have been obtained blending crystalline porous frameworks (MOFs or COFs) with polymeric matrixes to yield mixed matrix membranes.[34] In this regard, it has recently been shown that a COF-based mixed matrix membrane, obtained by impregnation of a COF (H_3PO_4@SNW-1) into a Nafion® matrix, exhibits a proton conductivity of 6.04×10^{-2} S cm^{-1} at 51% RH and 353 K.[35]

In order to study the reversibility of the **RT-COF-1Ac** and **LiCl@RT-COF-1** films *versus* moisture, we have carried out wetting-dewetting cycles. The reproducibility and consistency of the results was ensured using three different pellets for each material. Every cycle starts with a measurement of the conductivity value at 313 K and 22 % RH followed by the material wetting until the maximum conductivity value at 100 % RH is reached. Finally, the material is dried, for 12 h at 373 K, before the next cycle of measurements. As it can be appreciated in Figure S23, both materials respond in a reversible way after applying two wetting-dewetting cycles, reaching almost identical conductivity values at 100 % RH. Nevertheless, it has been found that in the case of the **RT-COF-1Ac** film (Figure S23a), the diffusion of water molecules through the structure becomes slower than that observed for the **LiCl@RT-COF-1** film, as a probable consequence of the lower hydrophilicity of the former material.

^{7}Li and ^{1}H static solid-state nuclear magnetic resonance (ssNMR) spectroscopy at 22 % and 100 % RH have let us corroborate the mobility of Li^+ and H^+ ions within the corresponding materials.[36] The highest relative humidity conditions were reached after placing the samples in a chamber saturated with water vapor and keeping them there for 15 min. to ensure the establishment of equilibrium state. Then, we have measured static ssNMR of ^{1}H and ^{7}Li and we have analyzed the

spectral line shapes since the width of the lines is dependent on the mobility of the studied ions. The change in the signal width (taken as the full width at half maximum - FWHM) is due to the solid-state dipole-dipole and quadrupolar interactions.[37]

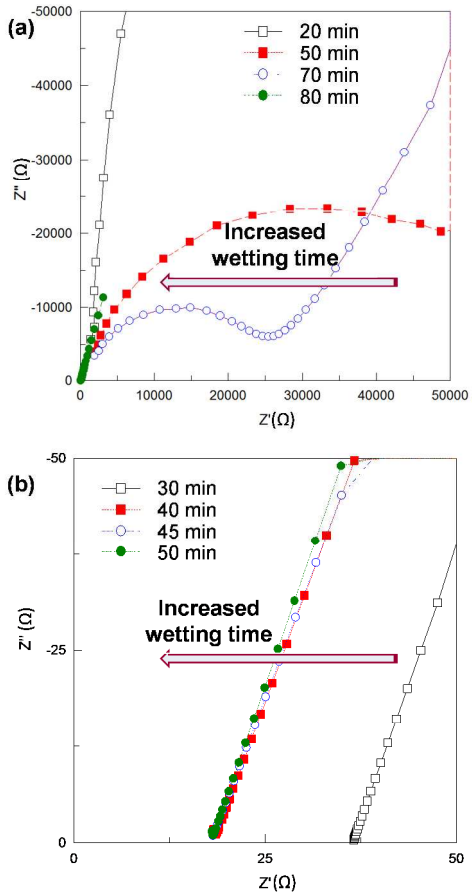

Figure 4. Nyquist plots for (a) **RT-COF-1AcB** and (b) **LiCl@RT-COF-1** films at 100 % RH and 313 K.

Table 1. Conductivity values at 313 K for the **RT-COF-1** pellet and **RT-COF-1Ac**, **RT-COF-1AcB** and **LiCl@RT-COF-1** films at 22 and 100% RH.

	σ, S cm^{-1} at 313 K	
	22% RH	100% RH
RT-COF-1	$< 1 \times 10^{-10}$	1.83×10^{-5}
RT-COF-1Ac	$< 1 \times 10^{-10}$	1.07×10^{-4}
RT-COF-1AcB	$< 1 \times 10^{-9}$	5.25×10^{-4}
LiCl@RT-COF-1	$< 1 \times 10^{-9}$	6.45×10^{-3}

When the nuclei are fixed, these interactions are emphasized, which results in a broad linewidth, commonly referred to as the rigid lattice linewidth. As the mobility of the cation increases, the NMR linewidth decreases due to the averaging of the interactions experienced by each nucleus.[38] Figure S8 shows the ^{7}Li ssNMR spectra obtained for **LiCl@RT-COF-1** at 22 % RH and 100 % RH and they are compared with the one obtained for dry LiCl (22 % RH). As it can be appreciated, the signal at 22 % RH for **LiCl@RT-COF-1** is very similar to LiCl and broader than the signal obtained at 100 % RH. It suggests that the mobility of the Li^{+} ions is significantly reduced at 22 % RH compared to 100 % RH. Similar trends are found in the ^{1}H ssNMR spectra for **RT-COF-1Ac**, **RT-COF-1AcB**, and **LiCl@RT-COF-1** at 100 % RH showing a sharp signal in every material indicative of high proton mobility (Figures S9). As expected, the narrower the signal the higher is the H^{+} mobility as concluded from the conductivity value measurements (Table 1 and Figure S9). Additionally, we have carried out pulse field gradient (PFG) NMR spectroscopy for ^{1}H and ^{7}Li in **LiCl@RT-COF-1** at 100 % RH in order to evaluate the diffusion of the H^{+} and Li^{+} ions into the cavities. For that, we have calculated the self-diffusion coefficient (D) of both active nuclei considering the model based on 1D diffusion along the channel.[39,40] The D of ^{1}H and ^{7}Li obtained for **LiCl@RT-COF-1** are 6.011×10^{-10} and 5.57×10^{-10} m^{2} s^{-1}, respectively, these are in agreement with those reported by Horike *et al.*[41] in their MOF modified post-synthetically with LiCl and similar to those of Nafion® 117, which is a popular H^{+} conductor ($D(^{1}H) = 8.0 \times 10^{-10}$ m^{2} s^{-1} exhibiting a conductivity value of 1.4×10^{-3} S cm^{-1} at 304 K and 40 % RH).[42] As in the case of the previously reported MOFs containing water in their cavities, we suggest that H^{+} hopping occurs in the COF channels of **RT-COF-1Ac**, **RT-COF-1Ac**, and **LiCl@RT-COF-1**.

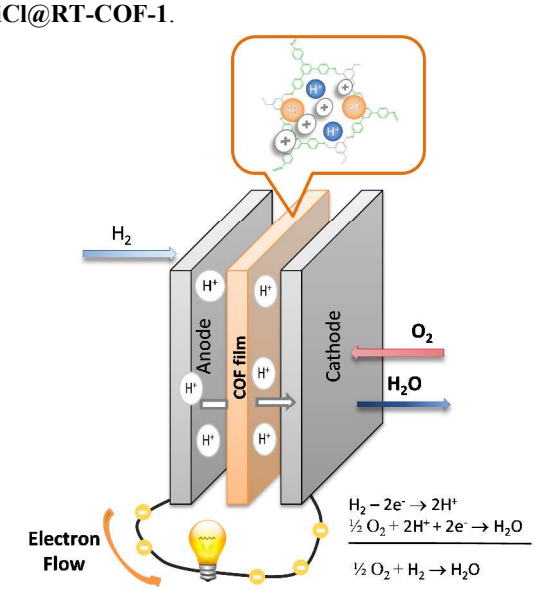

Figure 5. Scheme of the PEMFCs that uses **RT-COF-1Ac**, **RT-COF-1AcB** and **LiCl@RT-COF-1** films as membrane electrode assemblies (MEA).

Interestingly, the $D(^{7}Li)$ obtained for **LiCl@RT-COF-1**, which is comparable with that of H^{+}, indicates that Li^{+} also shows a fast diffusion in the COF channel. This result is a valuable information since the Nyquist plot of **LiCl@RT-COF-1** cannot distinguish H^{+} and Li^{+} conductivities. Therefore, these results agree with those found in a previously reported MOF containing water and LiCl in the cavity.[36] Therefore, it can be concluded that both ions have similar mobilities in the channel. We can assume that the hydrophilicity en-

hancement upon LiCl incorporation is also beneficial for improving the H^+ mobility, facilitating a Grotthuss mechanism.

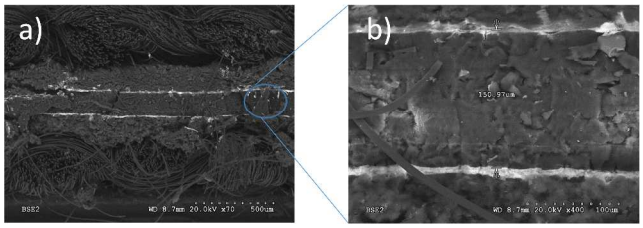

Figure 6. a) SEM micrograph of a MEA cross section with **RT-COF-1Ac** film as solid electrolyte. b) Zoom of the highlighted region in a).

Fuel Cell measurements. As mentioned above a general limitation of the COF materials for its implementation as fuel cells membranes is the lack of easy processability.[41] Taking all the above into consideration, we have selected **RT-COF-1Ac**, **RT-COF-1AcB** and **LiCl@RT-COF-1** films to study their ability as solid electrolytes for the construction of proof of concept proton-exchange membrane fuel cells (PEMFCs).

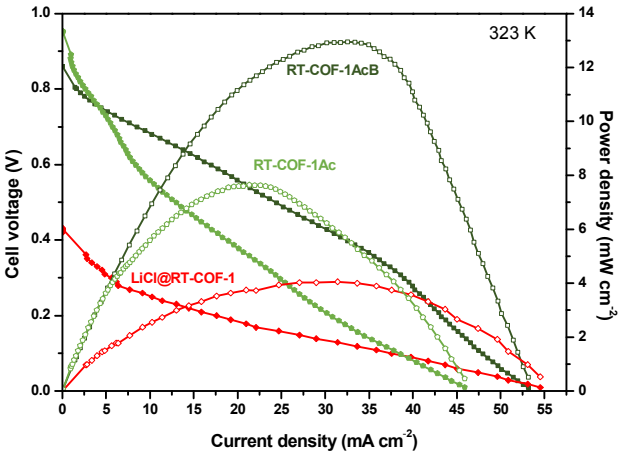

Figure 7. Polarization (filled symbols) and power density (open symbols) curves of **RT-COF-1Ac**, **RT-COF-1AcB** and **LiCl@RT-COF-1** films measured at 323 K for a single H_2/O_2 PEMFC.

Membrane electrode assemblies (MEAs) were prepared using the COF films as solid electrolytes and a commercial 40 wt. % Pt/C catalyst at both anode and cathode electrodes (Figures 5 and S24) and were characterized by SEM (Figures 6 and S18). The micrographs of **RT-COF-1Ac** confirm the formation of a uniform membrane with a thickness of ~160 µm (Figure 6). The compact packing of the proton electrolyte material is appreciated. This characteristic is necessary in order to have a good physical barrier for fuel gases separation, avoiding the fuel crossover and therefore the short circuit of the fuel cell. Consequently, the preliminary results were found to be very encouraging. MEAs with the different COF films show a starting open circuit potential (OCP) of 0.95 V, 0.88 V and 0.42 V at 323 K for **RT-COF-1Ac**, **RT-COF-1AcB** and **LiCl@RT-COF-1** films, respectively. The high OCP of **RT-COF-1Ac** and **RT-COF-1AcB** films demonstrates both the good ionic conductivity and mechanical properties of the **RT-COF-1Ac** film avoiding the H_2 crossover. On the other hand, the observed lower OCP of the MEA with **LiCl@RT-COF-1** film, at 323 K, might be indicative of the electrolyte suffering from poor mechanical properties, even after the addition of acetic acid during processing to improve the conformation of the film.

Polarization and power density curves of MEAs were also carried out in order to characterize the performance of the materials as fuel cell membranes and demonstrate *in situ* proton conductivity through the materials. Figure 7 gathers the fuel cell performance of the essayed MEAs at 323 K exhibiting maximum power density peaks at 12.95 mW cm^{-2}, 7.64 mW cm^{-2}, 4.06 mW cm^{-2} and maximum current density of 53.1 mA cm^{-2}, 45.9 mA cm^{-2} and 54.5 mA cm^{-2} for **RT-COF-1AcB**, **RT-COF-1Ac** and **LiCl@RT-COF-1** films, respectively. Furthermore, Figure S25 shows the result at 303 K. Although these performances are clearly inferior to that achieved by Nafion® based PEMFCs, representing state-of-the-art PEMFC technology, they are promising since they outperform previous reports for similar fuel cell membrane studies using naked COFs as solid electrolytes (Figure 8). Indeed, to the best of our knowledge only an imine based COF, named as PA@TpBpy, shows values for maximum power density of 7 mW cm^{-2} and current density of 29 mA cm^{-2} at 323 K,[41] which are below those found by **RT-COF-1AcB**. In this regard, as it is shown in Figure 8, only composite formation of COFs and MOFs leads to higher power density values pointing out the importance of improving the processability of COF materials by themselves in order to improve their performance.

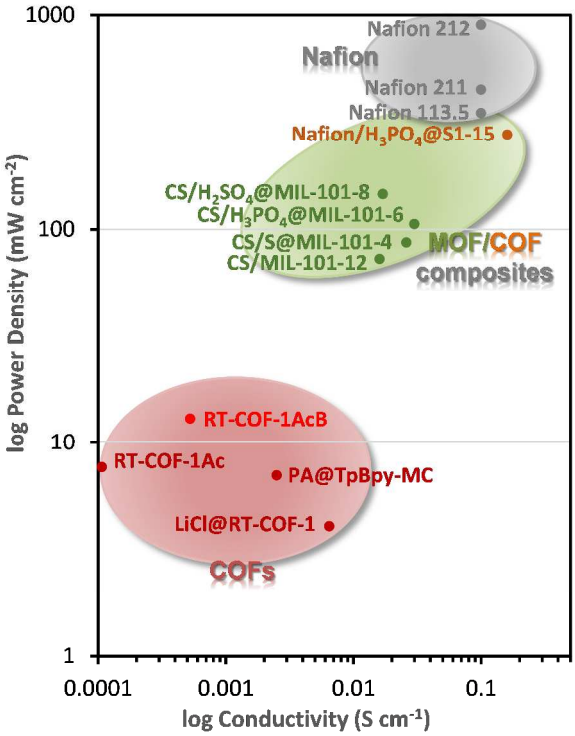

Figure 8. Comparison between conductivity versus power density values for COFs, representative MOF/COF-composites and different Nafions.[35,41,43-46]

Besides polarization curves, impedance spectroscopy was also used to characterize the performance of the essayed MEAs in operation at two different temperatures. Figure 9 and S26 shows Nyquist plots of the **RT-COF-1Ac**, **RT-COF-1AcB** and **LiCl@RT-COF-1** films measurements at 303 and 323 K, respectively. The influence of temperature is clearly visible, as it was noticed previously. Thus, for the **RT-COF-1Ac** MEA in the single cell the conductivity value at 303 K of 7.5×10^{-4} S cm^{-1} increases up to 4.6×10^{-3} S cm^{-1} at 323 K. Similarly the *in-situ* conductivity values at 323 K for **RT-COF-1AcB** and **LiCl@RT-COF-1** films are very high, namely 1.1×10^{-2} S cm^{-1} and 2.4×10^{-2} S cm^{-1}, respectively. These conductivity values are comparable with the previous results obtained in the *ex-situ* conductivity measurements although the experimental conditions, such as temperature, interphase of the cell configuration, SS/COF (conductivity *ex-situ*) *vs* Pt/COF (conductivity *in-situ*), or humidity (water is obtained as a reaction product in the fuel cell continuously) are slightly different.[41]

Despite the high conductivity value of the **LiCl@RT-COF-1** film, the polarization and power density curves are worse than those of **RT-COF-1Ac** and **RT-COF-1AcB**, which exhibit lower conductivity values. This result might be related to the worse processing features of the **LiCl@RT-COF-1** compared to the acetic acid processed ones. So, the results demonstrate that the catalytic activity and electrolytic features of acetic acid in the **RT-COF-1AcB** film give rise to an optimal balance of conductivity and mechanical properties yielding to the best performance in the PEMFC.

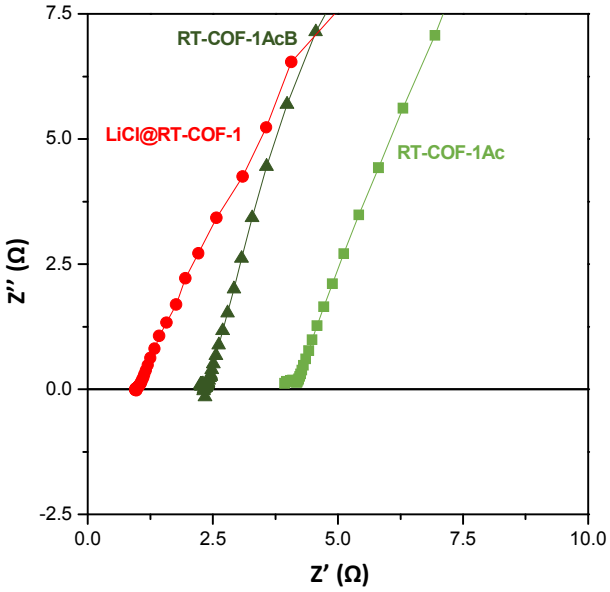

Figure 9. Nyquist diagrams of H_2(Pt)/COF film/(Pt)O_2 of fuel cells with **RT-COF-1Ac**, **RT-COF-1AcB** and **LiCl@RT-COF-1** films at 303 K.

Finally, in order to have information about the H_2 crossover in the PEMFC, linear sweep voltammetry was carried out according to the experimental set up included in SI. Figure 10 and S27 exhibit the current density *vs* potential curve from which the mass transfer limited current density (J_{lim}) was determined. This limiting current is related to the rate of H_2 crossover through the film employed as membrane by means of the equation:

$$J_{crossover\ H_2} = J_{lim}/nF$$

where n is 2, the number of electrons of the hydrogen oxidation reaction and F is Faraday's constant (96485 C electron-mol^{-1}).

Using this equation, the H_2 crossover ratios are 2.6×10^{-8} mol cm^{-2}s^{-1}, 3.2×10^{-8} mol cm^{-2}s^{-1} and 3.7×10^{-8} mol cm^{-2}s^{-1} for **RT-COF-1AcB**, **RT-COF-1Ac** and **LiCl@RT-COF-1** films, respectively, not outperforming Nafion® membranes (~10^{-9} mol cm^{-2}s^{-1})[47,48] but still slightly below the 4.1×10^{-8} mol cm^{-2}s^{-1} values reported by Shinde et *al.*[41] in related COFs. The much lower H_2 crossover corroborates the better mechanical properties of **RT-COF-1Ac** and **RT-COF-1AcB** films compared to **LiCl@RT-COF-1** films. These values are also comparable to commercial Nafion® 117 PEMFC with similar thickness (~177 µm) and after several hours of operation. It is expected a better behavior with lower thickness as found in Nafion® 112 H_2/O_2 PEMFC exhibiting 50 µm thickness.

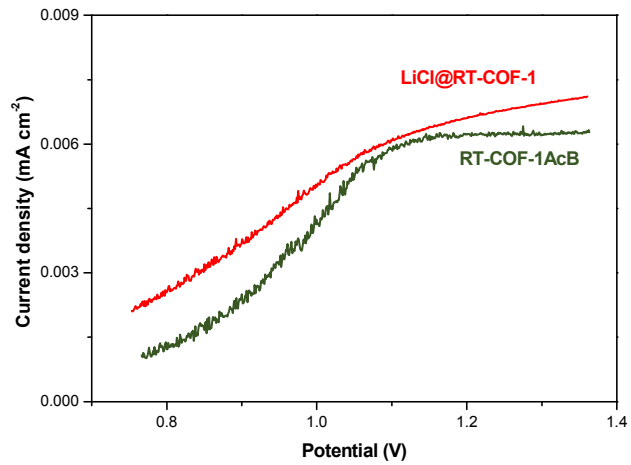

Figure 10. Lineal Sweep Voltamogramm for hydrogen crossover in MEA with **RT-COF-1AcB** and **LiCl@RT-COF-1** films as electrolytes after 6 hours.

Conclusions

A series of imine-based COFs incorporating different guest molecules in their cavities (H_2O, HAcO, LiCl) leads to materials showing remarkable high ionic conductivity, e.g. when HAcO or LiCl are incorporated. The resulting materials are highly hydrophilic giving rise to a high ionic conductivity improvement upon exposure to moisture (up to 6.45×10^{-3} S cm^{-1} at 313 K), pointing towards a water mediated conduction mechanism (i.e. Grotthuss). Noteworthy, we have found that the COF materials can be processed in the form of films allowing their integration as solid electrolyte membranes in Fuel Cells. Overall, the **RT-COF-1AcB** film exhibits the best performance, which is related to an optimal balance between mechanical properties (leading to low H_2 fuel crossover) and high conductivity values under operating conditions (1.1×10^{-2} S cm^{-1} at 323 K) that leads to a maximum power density peak at 12.95 mW cm^{-2} and a maximum current density of 53.1 mA cm^{-2}. To the best of our knowledge, the results obtained show

that the acetic acid processed **RT-COF-1Ac** and **RT-COF-1AcB** films have good performances and are among the best values in state-of-the-art ion exchange membranes based only on naked COFs materials for the construction of PEMFCs. We believe that there is still a large playground to improve the performance of COFs based ion exchange membranes in order to approach the values of current state-of-the-art technology.

ASSOCIATED CONTENT

Supporting Information. Additional experimental data and characterization details are provided as Supporting Information. This material is available free of charge via the Internet at http://pubs.acs.org.

AUTHOR INFORMATION

Corresponding Author

* E-mail: felix.zamora@uam.es

Author Contributions

The manuscript was written through contributions of all authors. All authors have given approval to the final version of the manuscript.

ACKNOWLEDGMENT

We thank the MINECO (Spain) for financial support through Juan de la Cierva postdoctoral fellowship. We thank the Spanish Ministry of Economy (MAT2016-77608-C3-1-P, MAT2013-46753-C2-1-P, CTQ2014-53486-R, ENE2016-77055-C3-1-R), and Comunidad de Madrid (S2013/MAE-2882) for generous funding.

REFERENCES

(1) Neto, A. O.; Giz, M. J.; Perez, J.; Ticianelli, E. A.; Gonzalez, E. R. *J. Electrochem. Soc.* **2002**, *149*, A272.
(2) Nataraj, S. K.; Wang, C. H.; Huang, H. C.; Du, H. Y.; Wang, S. F.; Chen, Y. C.; Chen, L. C.; Chen, K. H. *Chemsuschem.* **2012**, *5*, 392.
(3) Slade, R. C. T.; Varcoe, J. R. *Solid State Ionics* **2005**, *176*, 585.
(4) Hernández-Flores, G.; Poggi-Varaldo, H. M.; Solorza-Feria, O. *Int. J. Hydrogen Energy* **2016**, *41*, 23354.
(5) Hickner, M. A.; Ghassemi, H.; Kim, Y. S.; Einsla, B. R.; McGrath, J. E. *Chem. Rev.* **2004**, *104*, 4587.
(6) Meng, X.; Wang, H.-N.; Song, S.-Y.; Zhang, H.-J. *Chem. Soc. Rev.* **2017**, *46*, 464.
(7) Kreuer, K. D. *J. Membr. Sci.* **2001**, *185*, 29.
(8) Côté, A. P.; Benin, A. I.; Ockwig, N. W.; O'Keeffe, M.; Matzger, A. J.; Yaghi, O. M. *Science* **2005**, *310*, 1166.
(9) Feng, X.; Ding, X.; Jiang, D. *Chem. Soc. Rev.* **2012**, *41*, 6010.
(10) Segura, J. L.; Mancheno, M. J.; Zamora, F. *Chem. Soc. Rev.* **2016**, *45*, 5635.
(11) Ding, S.-Y.; Wang, W. *Chem. Soc. Rev.* **2013**, *42*, 548.
(12) Colson, J. W.; Dichtel, W. R. *Nat. Chem.* **2013**, *5*, 453.
(13) Xu, H.; Gao, J.; Jiang, D. *Nat. Chem.* **2015**, *7*, 905.
(14) Huang, N.; Wang, P.; Jiang, D. *Nat. Rev. Mater.* **2016**, *1*, 16068.
(15) Chandra, S.; Kundu, T.; Dey, K.; Addicoat, M.; Heine, T.; Banerjee, R. *Chem. Mater.* **2016**, *28*, 1489.
(16) Ma, H.; Liu, B.; Li, B.; Zhang, L.; Li, Y.-G.; Tan, H.-Q.; Zang, H.-Y.; Zhu, G. *J. Am. Chem. Soc.* **2016**, *138*, 5897.
(17) Vazquez-Molina, D. A.; Mohammad-Pour, G. S.; Lee, C.; Logan, M. W.; Duan, X.; Harper, J. K.; Uribe-Romo, F. J. *J.Am. Chem. Soc.* **2016**, *138*, 9767.
(18) Chandra, S.; Kundu, T.; Kandambeth, S.; BabaRao, R.; Marathe, Y.; Kunjir, S. M.; Banerjee, R. *J. Am. Chem. Soc.* **2014**, *136*, 6570.
(19) Peng, Y.; Xu, G.; Hu, Z.; Cheng, Y.; Chi, C.; Yuan, D.; Cheng, H.; Zhao, D. *ACS Appl. Mater. Interf.* **2016**, *8*, 18505.
(20) de la Peña Ruigómez, A.; Rodríguez-San-Miguel, D.; Stylianou, K. C.; Cavallini, M.; Gentili, D.; Liscio, F.; Milita, S.; Roscioni , O. M.; Ruiz-González, M. L.; Carbonell, C.; Maspoch, D.; Mas-Ballesté, R.; Segura, J. L.; Zamora, F. *Chem. Eur. J.* **2015**, *21*, 10666.
(21) Kandambeth, S.; Mallick, A.; Lukose, B.; Mane, M. V.; Heine, T.; Banerjee, R. *J. Am. Chem. Soc.* **2012**, *134*, 19524.
(22) Biswal, B. P.; Chandra, S.; Kandambeth, S.; Lukose, B.; Heine, T.; Banerjee, R. *J. Am. Chem. Soc.* **2013**, *135*, 5328.
(23) Rodriguez-San-Miguel, D.; Abrishamkar, A.; Navarro, J. A. R.; Rodriguez-Trujillo, R.; Amabilino, D. B.; Mas-Balleste, R.; Zamora, F.; Puigmarti-Luis, J. *Chem. Commun.* **2016**, *52*, 9212.
(24) Calik, M.; Auras, F.; Salonen, L. M.; Bader, K.; Grill, I.; Handloser, M.; Medina, D. D.; Dogru, M.; Löbermann, F.; Trauner, D.; Hartschuh, A.; Bein, T. *J. Am. Chem. Soc.* **2014**, *136*, 17802.
(25) Medina, D. D.; Rotter, J. M.; Hu, Y.; Dogru, M.; Werner, V.; Auras, F.; Markiewicz, J. T.; Knochel, P.; Bein, T. *J. Am. Chem. Soc.* **2015**, *137*, 1016.
(26) Tabares, L. C.; Navarro, J. A. R.; Salas, J. M. *J. Am. Chem. Soc.* **2001**, *123*, 383.
(27) Sadakiyo, M.; Yamada, T.; Kitagawa, H. *J. Am. Chem. Soc.* **2009**, *131*, 9906.
(28) Bazaga-García, M.; Colodrero, R. M. P.; Papadaki, M.; Garczarek, P.; Zoń, J.; Olivera-Pastor, P.; Losilla, E. R.; León-Reina, L.; Aranda, M. A. G.; Choquesillo-Lazarte, D.; Demadis, K. D.; Cabeza, A. *J. Am. Chem. Soc.* **2014**, *136*, 5731.
(29) Xu, G.; Otsubo, K.; Yamada, T.; Sakaida, S.; Kitagawa, H. *J. Am. Chem. Soc.* **2013**, *135*, 7438.
(30) Panda, T.; Kundu, T.; Banerjee, R. *Chem. Commun.* **2012**, *48*, 5464.
(31) Panda, T.; Kundu, T.; Banerjee, R. *Chem. Commun.* **2013**, *49*, 6197.
(32) Mauritz, K. A.; Moore, R. B. *Chem. Rev.* **2004**, *104*, 4535.
(33) Xu, H.; Tao, S.; Jiang, D. *Nat. Mater.* **2016**, *15*, 722.
(34) Ivanova, A. G.; Il'in, P. A.; Dmitrieva, A. A.; Zagrebelnyy, O. A.; Gruzinov, A. Y.; Kopitsa, G. P.; Kruchinina, I. Y.; Shilova, O. A. *Glass Phys. Chem.* **2016**, *42*, 637.
(35) Yin, Y.; Li, Z.; Yang, X.; Cao, L.; Wang, C.; Zhang, B.; Wu, H.; Jiang, Z. *J. Power Sources* **2016**, *332*, 265.
(36) Horike, S.; Kamitsubo, Y.; Inukai, M.; Fukushima, T.; Umeyama, D.; Itakura, T.; Kitagawa, S. *J. Am. Chem. Soc.* **2013**, *135*, 4612.
(37) Pople, J. A.; Schneider, W. G.; Bernstein, H. J. *J. Chem. Educ.* **1960**, *37*, A322.
(38) Every, H. A.; Zhou, F.; Forsyth, M.; MacFarlane, D. R. *Electrochim. Acta* **1998**, *43*, 1465.
(39) Ray, M. S. *Dev. Chem. Eng. Min.* **1996**, *4*, 254.
(40) Chmelik, C.; Karger, J. *Chem. Soc. Rev.* **2010**, *39*, 4864.
(41) Shinde, D. B.; Aiyappa, H. B.; Bhadra, M.; Biswal, B. P.; Wadge, P.; Kandambeth, S.; Garai, B.; Kundu, T.; Kurungot, S.; Banerjee, R. *J. Mater. Chem. A* **2016**, *4*, 2682.
(42) Ochi, S.; Kamishima, O.; Mizusaki, J.; Kawamura, J. *Solid State Ionics* **2009**, *180*, 580.
(43) Dong, X.-Y.; Li, J.-J.; Han, Z.; Duan, P.-G.; Li, L.-K.; Zang, S.-Q. *J. Mater. Chem. A* **2017**, *5*, 3464.
(44) Liu, W.; Xie, Y.; Liu, J.; Jie, X.; Gu, J.; Zou, Z. *Int. J. Hydrogen Energy* **2012**, *37*, 4673.
(45) Wang, L.; Yi, B. L.; Zhang, H. M.; Xing, D. M. *Electrochim. Acta* **2007**, *52*, 5479.
(46) Escudero-Cid, R.; Varela, A. S.; Hernández-Fernández, P.; Fatás, E.; Ocón, P. *Int. J. Hydrogen Energy* **2014**, *39*, 5063.
(47) Ye, D.; Tu, Z.; Yu, Y.; Cai, Y.; Zhang, H.; Zhan, Z.; Pan, M. *Int. J. Energy Res.* **2014**, *38*, 1181.

(48) Schalenbach, M.; Hoefner, T.; Paciok, P.; Carmo, M.; Lueke, W.; Stolten, D. *J. Phys. Chem. C* **2015**, *119*, 25145.

Table of Contents artwork